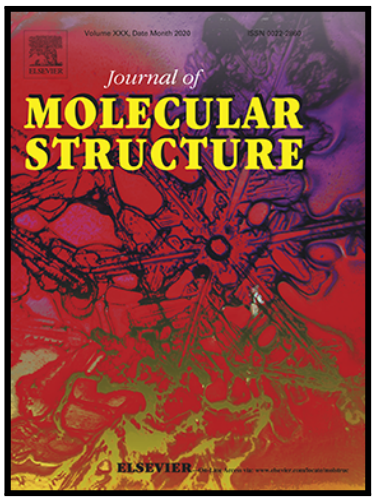

Synthesis and spectroscopic characterization of Fe^{3+}-BDC metal organic framework as material for lithium ion batteries

Cesario Ajpi , Naviana Leiva , Anders Lundblad , Göran Lindbergh , Saul Cabrera

PII: S0022-2860(22)01778-1
DOI: https://doi.org/10.1016/j.molstruc.2022.134127
Reference: MOLSTR 134127

To appear in: *Journal of Molecular Structure*

Received date: 9 April 2022
Revised date: 30 August 2022
Accepted date: 7 September 2022

Please cite this article as: Cesario Ajpi , Naviana Leiva , Anders Lundblad , Göran Lindbergh , Saul Cabrera , Synthesis and spectroscopic characterization of Fe^{3+}-BDC metal organic framework as material for lithium ion batteries, *Journal of Molecular Structure* (2022), doi: https://doi.org/10.1016/j.molstruc.2022.134127

Synthesis and spectroscopic characterization of Fe^{3+}-BDC metal organic framework as material for lithium ion batteries

Cesario Ajpi[1,3], Naviana Leiva[1], Anders Lundblad[2], Göran Lindbergh[3], Saul Cabrera[1]

[1]Department of Inorganic Chemistry and Materials Science/Advanced Materials, IIQ Chemistry Research Institute, UMSA Universidad Mayor de San Andres, La Paz, Bolivia
[2] Division of Safety and Transport/Electronics, RISE, Research Institutes of, Sweden, SE-504 62 Borås, Sweden
[3] Department of Chemical Engineering, Applied Electrochemistry, KTH Royal Institute of Technology, SE-100 44 Stockholm, Sweden
cesario.ajpi@gmail.com

Keywords: Structure, metal organic frameworks, lithium-ion batteries.

Highlights

The synthetized mixture of Fe-MOFs were characterized by XRD.

The spectroscopic properties of the Fe-MOFs were investigated by IR.

The electrochemical properties of the Fe-MOFs were investigated by CV , EIS and charge-discharge methods.

The cavities and channels were calculated and used in order to predict the possible accommodation sites for Li^+ ions.

The possible interactions of Li^+ were described in the structures of Fe-MOFs compounds.

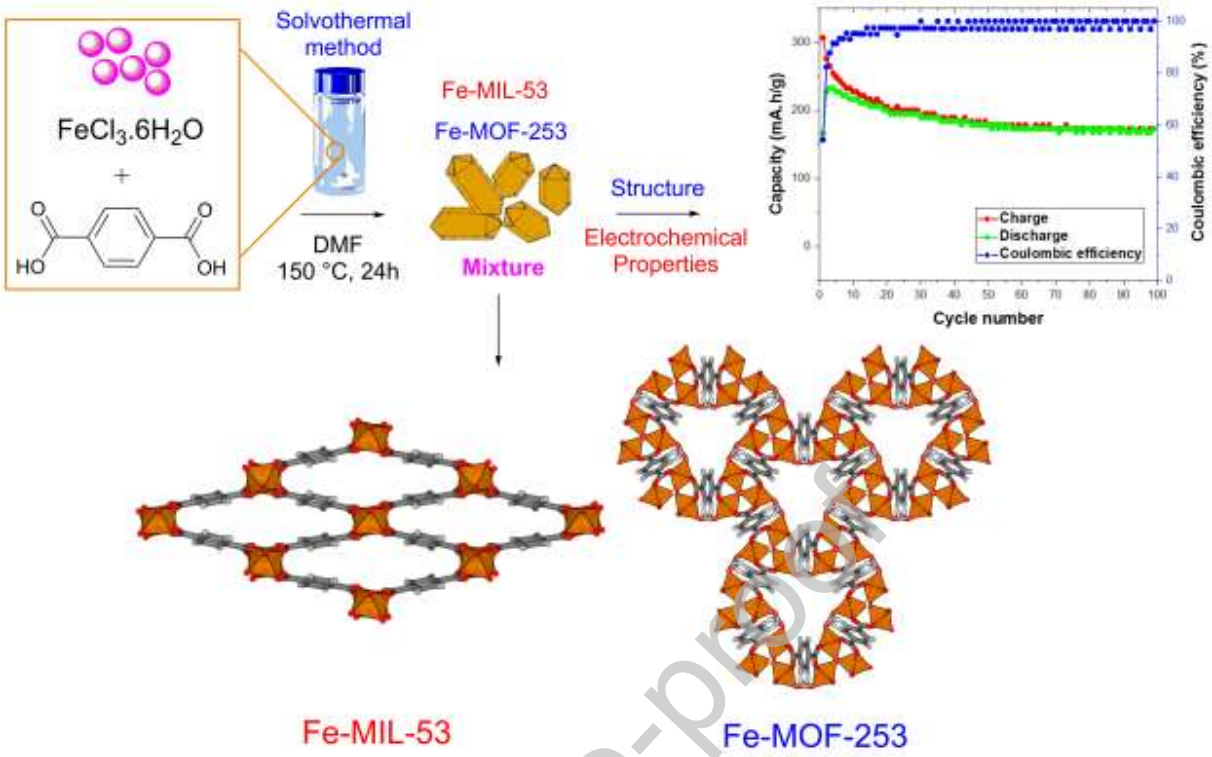

This work presents synthesis and spectroscopic characterization of a new metal-organic framework (MOF). The compound Fe-BDC-DMF was synthetized by the solvothermal method and prepared via a reaction between $FeCl_3 \cdot 6H_2O$ and benzene-1,4-dicarboxylic acid (H_2BDC) or terephthalic acid using N,N-dimethylformamide (DMF) as solvent. The powder was characterized by powder X-ray diffraction (PXRD), scanning electron microscopy (SEM) and infrared spectroscopy (IR) analysis. The electrochemical properties were investigated in a typical lithium-ion battery electrolyte by cyclic voltammetry (CV), electrochemical impedance spectroscopy (EIS) and galvanostatic charging and discharging.

The synthetized Fe-BDC-DMF metal-organic framework (MOF) contains a mixture of three phases, identified by PXRD as: MOF-235, and MIL-53(Fe) monoclinic with C2/c and P21/c space groups. The structure of the Fe-BDC is built up from Fe^{3+} ions, terephalates (BDC) bridges and in-situ-generated DMF ligands.

The electrochemical measurements conducted in the potential range of 0.5–3.5 V vs. Li^+/Li^0 show the voltage profiles of Fe-BDC and a plateau capacity of around 175 mAh/g.

1. INTRODUCTION

Hybrid materials can be defined as materials with inorganic and organic components homogeneously distribution on a molecular level. The metal-organic framework (MOF) is a kind of such hybrid material [1].

The structures of MOFs are built from metal coordination centers or oxy-clusters and linked by organic ligands forming three dimensional (3D) extended structures with considerable porosity. The MOFs can possess large surface areas up to around 6000 m^2/g [2-3] and be multifunctional materials with different applications in separation and sorption, showing better properties compared with the traditional zeolites. Other applications are hydrogen [4-6] and carbon dioxide storage [7-8] for energy and environmental purposes, and the use in other areas such as catalysis and electrode materials for energy storage [9].Metal organic frameworks (MOFs) also have shown to work efficiently for adsorption of dyes owing to their porous structure [10-11] and gas adsorption as N_2, H_2, CO_2 and CH_4 [12].

The main structural feature of the MOFs is their tunability from micro- to mesoporosity, determined by the organic linker, which makes it possible to control the size of the pores. The MIL-n family (MIL = Materials of Institut Lavoisier) have illustrated these ideas by combining simple octahedral metal clusters with organic carboxylates. The porous structures formed have remarkable properties when a simple guest molecule is introduced into the structure, resulting in reversible expansion-contraction of the unit cell volumes [13].

The synthesis of metal-organic frameworks (MOFs), coordination polymers (CPs) and coordination networks (CNs) depends on many factors, such as the metal ions, organic linkers, solvents, temperature, and pH [14-16]. The metal ions and organic ligands are especially important for the design because they define the metal nodes and the organic structures [17-18] and will define the type of the metal-organic compound formed. An effective method for the design and regulation of the properties of MOFs, CPs and CNs is the selection of organic linkers [19].

According to Scherb et al. [20] the synthesis of Fe-BDC can occur by homogeneous nucleation and heterogeneous nucleation. In the system Fe^{3+}/BDC, Fe-MIL-53 is the product of homogeneous nucleation while oriented Fe-MIL-88B is the product of heterogeneous nucleation.

Thanks to good thermal stability, up to 300 °C for Fe-MIL-53 [21-23] and up to 500 °C for Fe-MOF-253 [24], these materials show an excellent structure stability and can be interesting as anodes for lithium ion batteries [25-26].

In this work, a Fe^{3+} cation, terephthalic acid (H_2BDC) as linker and N,N-dimethyl formamide (DMF) as solvent and linker have been used to synthesize a Fe-MOF. The crystallographic structures of the Fe-MOFs are presented together with spectroscopy characterizations. Furthermore, electrochemical properties were characterized to investigate its potential as active material for lithium-ion batteries.

2. EXPERIMENTAL

Synthesis of Fe^{3+}-BDC-DMF

The compound was synthetized by the solvothermal method through the reaction between $FeCl_3\,6H_2O$ (0.7037g), terephthalic acid (H_2BDC) (0.8651g) and N,N-dimethylformamide (DMF) (50 ml) as a solvent. In the synthesis, the molar ratio was 1:1 of the Fe^{3+}:H_2BDC. The

reactants were dissolved in DMF, and subsequently the solution was transferred to a steel autoclave and heat treated at 150 °C for 24 h, according to Scheme I.

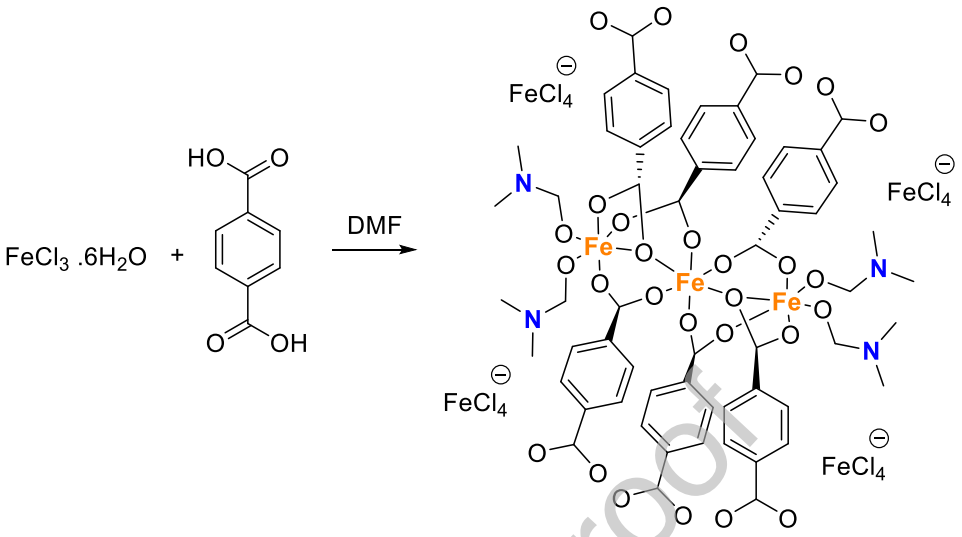

Scheme I. The schematic reaction of the synthesis used in this study.

The orange powder crystals were collected by filtration, washed several times with DMF and dried at 100 °C. The yield of the collected orange powder crystals was 0.4954 g, corresponding to 50%. The chemicals and solvents used for the synthesis were of reagent grade and were used without further purification.

The Fe-BDC-DMF was characterized by powder X-ray diffraction (PXRD) using an X'Pert3 PANalytical, with a scan rate of 0.02 °/s and Cu–Kα radiation (λ = 1.5406 Å). X'pert Highscore software (PANalytical. B. V, Lelyweg, the Netherlands) was used for identification of the phases. The morphologies of the samples were determined by S-4800 series field-emission high-resolution scanning electron microscope (SEM) (Hitachi, Tokyo, Japan), equipped with EDS detector (Oxford Instruments, UK). The powder samples were mounted in the sample holder and sputtered with a thin layer of Pt/Pd. The Fourier transform infrared spectroscopy (FTIR) was carried out on a Spectrum 100 (Perkin Elmer) in the wavelength range of 4000–400 cm^{-1} with a resolution of 1 cm^{-1}.

Electrochemical procedure

The Fe-BDC-DMF powder was used to prepare electrodes by dispersing the active material, carbon super P, and poly(vinylidene fluoride) (PVDF) binder in a composition of 80:10:10 wt% in 1-methyl-2-pyrrolidinone (NMP) solvent, with the mixture ground until it became homogeneous, using an agate mortar. The resulting slurry was pasted onto a copper foil and dried in vacuum at 90 °C for 24 h to remove the NMP solvent. An electrode disc with a diameter of 14 mm was cut out and cells were fabricated to test the charge/discharge performance according to the scheme presented in Fig. 1. The cells were assembled in an argon-filled glove box (H_2O, O_2 < 0.1 ppm). The electrolyte was 1 M $LiPF_6$ in a mixture of ethylene carbonate (EC)

and dimethyl carbonate (DMC) (1:1 by volume) and microporous polypropylene film (Celgard 2325) was used as separator.

The electrochemical characterization by cyclic voltammetry (CV), electrochemical impedance spectroscopy (EIS) and charge-discharge curves were recorded with a Gamry 600 potentiostat. The electrochemical impedance was measured at 1 mHz – 1MHz and an AC voltage amplitude of 10 mV. The cyclic voltammograms were recorded with a scan rate of 10 mV/s at 20 °C. The charge and discharge curves were recorded at a rate of 30 mA/g in the potential window 0.5–3.5 V vs. Li^+/Li^0.

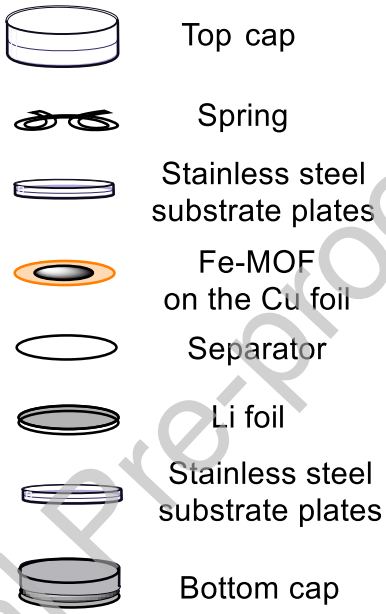

Figure 1. Schematic diagram of a coin cell with the active materials (Fe-BDC-carbon super P-PVDF electrode).

4. RESULTS AND DISCUSSION

XRD characterizations

The orange powder obtained as product after the synthesis was characterized by powder X-ray diffractometry (PXRD). The diffraction pattern is shown in Fig 2. In order to further identify the phases a Rietveld refinement of the X-ray powder diffraction pattern was performed using Xpert-high Score v.3.0 program. The CIFs used in the refinement were MOF-235 ($[Fe_3O(1,4\text{-}BDC)_3(DMF)_3][FeCl_4]*(DMF)_3$) reported by Sudik et al. [27] in the supporting information, and MIL-53(Fe) ($Fe^{III}(OH)\{O_2C\text{-}C_6H_4\text{-}CO_2\}*H_2O$) and ($Fe^{III}(OH)\{O_2C\text{-}C_6H_4\text{-}CO_2\}$) reported by Millange et al. [28] as supplementary files. A pseudo-Voigt function convoluted with an axial divergence symmetry function was used to model the peak profile of Fe-BDC-DMF. The lattice parameters and profile parameters were refined by atomic positions and anisotropic displacement

parameters. The simulated XRD pattern coincide well with the measured XRD pattern. The Rietveld refinement plot is shown in Fig. 2 and Table 1.

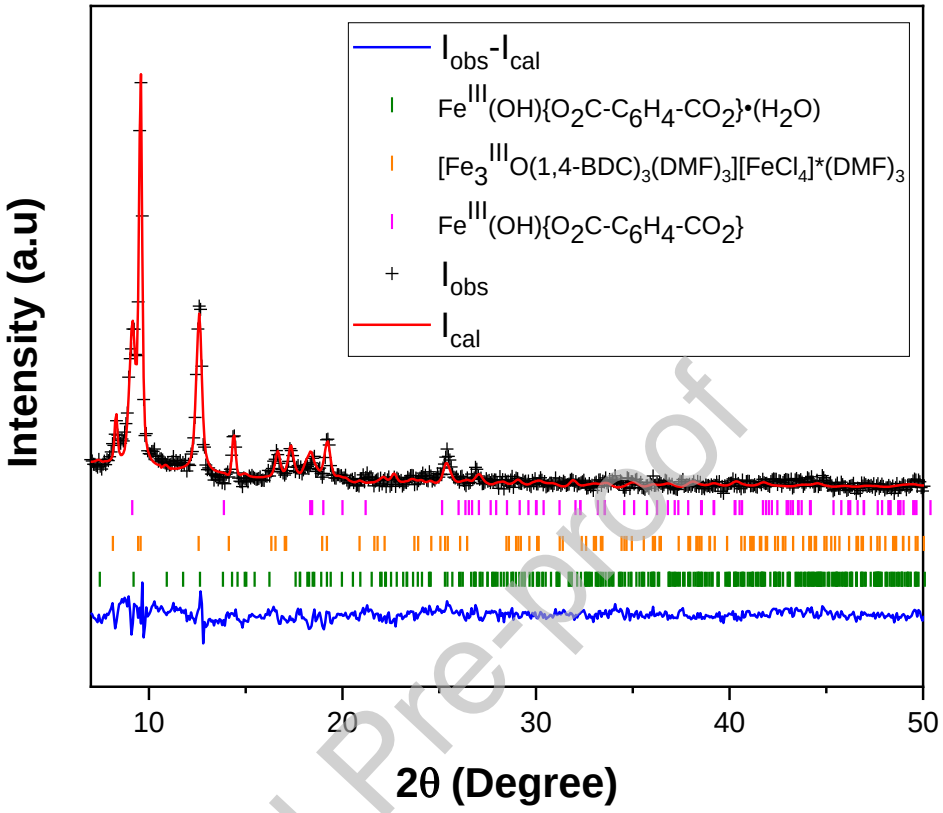

Figure 2. Diffraction pattern and Rietveld refined intensity pattern of the Fe-BDC-DMF sample.

The agreement indices were satisfactory between the calculated and the observed intensities and the structure of the phases identified are:

Phase 1 ($[Fe_3O(1,4\text{-}BDC)_3(DMF)_3][FeCl_4]*(DMF)_3$)(34.7%)

Phase 2 ($Fe^{III}(OH)\{O_2C\text{-}C_6H_4\text{-}CO_2\}$)(5.8%)

Phase 3 ($Fe^{III}(OH)\{O_2C\text{-}C_6H_4\text{-}CO_2\}*H_2O$).(59.5%)

Table 1. Details of Rietveld refined PXRD parameters for Fe-BDC-DMF

Parameters	**Phase 1**	**Phase 2**	**Phase 3**
2θ range (deg.)	05–70°	05–70°	05–70°
Step size (deg.)	0.0710°	0.0710°	0.0710°
Wavelength	1.5406 Å	1.5406 Å	1.5406 Å
Zero point (2θ,°)	0.000102	0.000102	0.000102
Pseudo-Voigt function $pV(x) = \eta C(x) + (1 - \eta)G(x)$	η = 0.60	η = 0.60	η = 0.60

Parameters	**Phase 1**	**Phase 2**	**Phase 3**
Space group	Hexagonal *P-62c*	Monoclinic *C2/c*	Monoclinic $P2_1/c$
a (Å)	12.24306	18.94696	19.34017
b (Å)	12.24306	6.51154	15.06246
c (Å)	18.51086	6.97578	6.96892
α(°)	90	90	90
β (°)	90	103.1824	94.99618
γ (°)	120	90	90
Volume (Å^3)	2402.909	837.95	2022.408
R_{Bragg}	1.08	0.85	1.16
R_{wp}	3.16	3.16	3.16
R_{exp}	2.21	2.21	2.21
R_p	2.44	2.44	2.44
GOF	2.03	2.03	2.03

The structures of the identified phases are show in Figure 3.

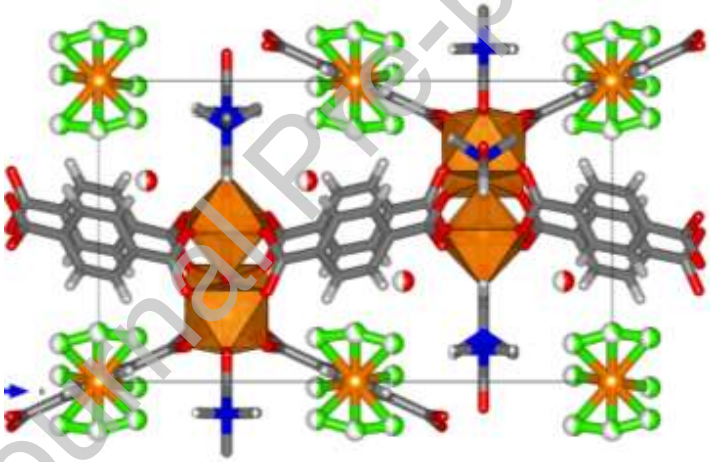

3a. Structure of Phase 1

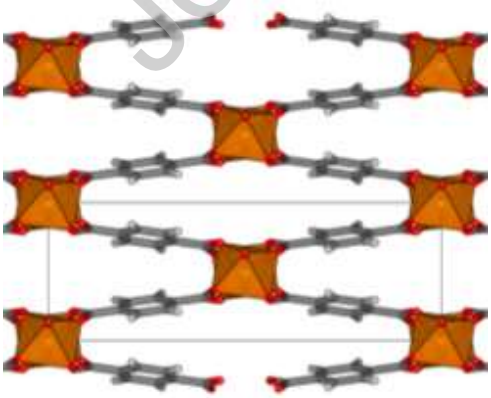

3b. Structure Phase 2

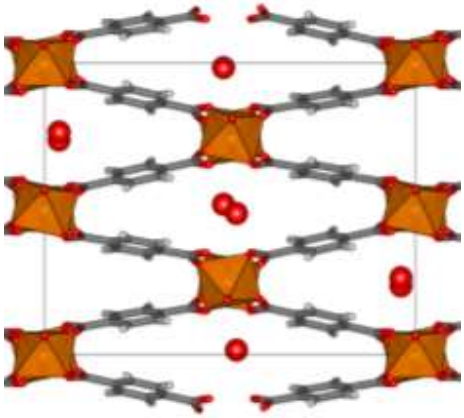

3c. Structure Phase 3

Figure 3. Structures of the phases, 3a. Structure of Phase 1 ($[Fe_3O(1,4\text{-}BDC)_3(DMF)_3][FeCl_4]^*(DMF)_3$), 3b. Structure of Phase 2 ($Fe^{III}(OH)\{O_2C\text{-}C_6H_4\text{-}CO_2\}$), 3c. Structure of Phase 3 ($Fe^{III}(OH)\{O_2C\text{-}C_6H_4\text{-}CO_2\}^*H_2O$).

The simulated XRD pattern using the CIFs coincide well with the measured XRD pattern shown in Fig. 4. Ex-situ XRD of pristine Fe-BDC and od the material in the electrode after 100 cycles were performed to investigate the electrochemical reversibility and the structural changes during the charge-discharge processes.

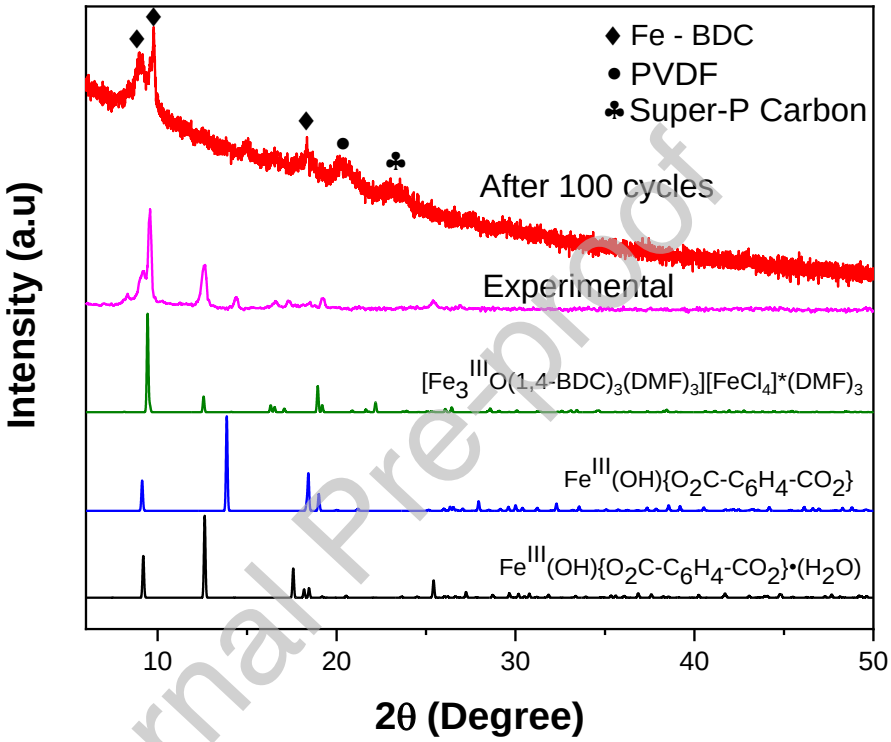

Figure. 4. Ex-situ XRD patterns of experimental simulated from CIFs and after 100 cycles (green = Phase 1, blue = Phase 2, black = Phase 3)

The XRD profile after 100 cycles have features of the pristine material but indicates changes in the structure of Phase 3 during the charge-discharge process. However, the data show good stability for the structure of Phase 1 and Phase 2. The XRD profile also shows an amorphous phase which is attributed to the Super P carbon and PVDF. The peaks at 21° corresponds to PVDF and the peak at 24° correspond to amorphous carbon Super-P. The peak at 12.7° disappear in the cycled sample. It corresponds to the (1,2,0) crystallographic plane of Phase 3, which contains the O atoms of the water molecules labeled by Ow1 and Ow2. The disappearance of this peak can be attributed to loss of the water molecule in the structure by the reaction with the electrolyte:

$$LiPF_6 + 4H_2O \longrightarrow LiF + H_3PO_4 + 5HF \quad (1)$$

Figure. 5 is showing the crystallographic plane (1,2,0) in the structure of the Phase 3.

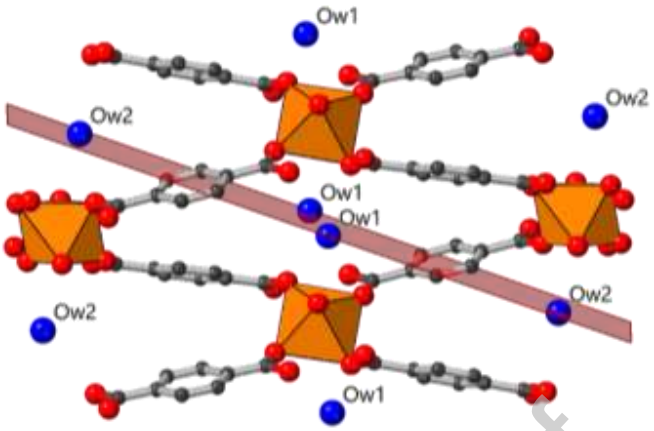

Figure. 5. Structure of Phase 3, showing the H_2O molecules (Ow1 and Ox2) and the plane (1,2,0).

Phase 1 and Phase 2 do not show any significant changes in the structure, indicating good stability of their structures in the charge-discharge processes.

Synthesis products of Fe^{3+}-BDC-DMF

According to Scherb et al. [20], the reaction products of the system Fe^{3+}:H_2BDC are depending on the nucleation process, which can be homogenous or heterogeneous. Fe-MIL-53 is the product of homogeneous nucleation and Fe-MOF-235 is the product of heterogeneous nucleation.

The XRD analysis suggests that the synthesis products of Fe-BDC are a mixture of the monoclinic structure of Fe(OH)(BDC) and Fe(OH)(BDC)(H_2O), analogues of MIL-53. The chains of FeO_6-octahedrals are connected by 1,4-benzenedicarboxylate anions in one-dimensional (1D) channels in the structure. The hexagonal three-dimensional (3D) structure of MOF-235 is an analogue to MIL-88B.It is built up from trinuclear Fe complexes of FeO_6-octahedrals linked to one oxygen and the trinuclear Fe, which in turn is linked to 1,4-benzenedicarboxylate anions with other trinuclear Fe complexes. The structure forms channels that are connected by bipyramidal cages, as shown in Scheme II, giving the 3D pore system of MOF-235 and MIL-88B.

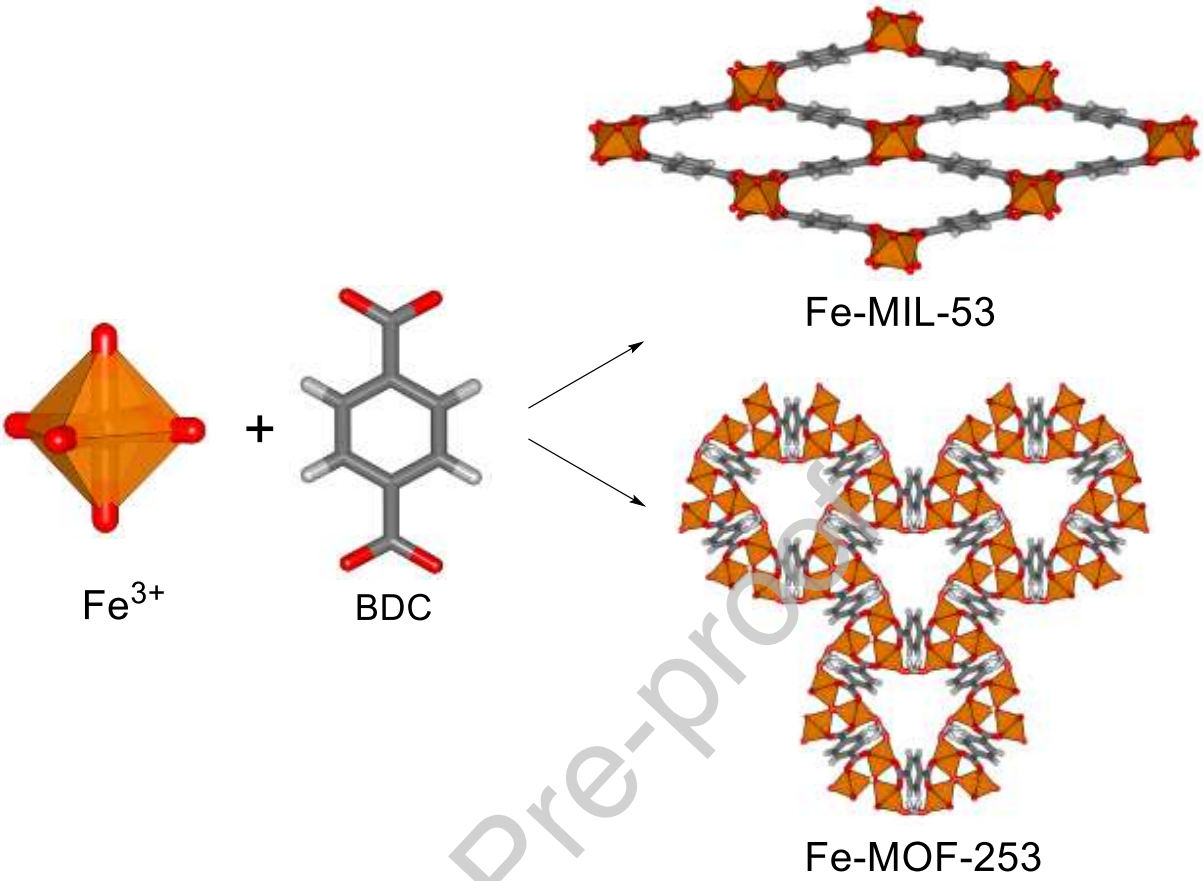

Scheme II. The schematic reaction of the synthesis used in this study where Fe-MIL-53 is the product of heterogenous nucleation and Fe-MOF-253 is the product of homogenous nucleation.

SEM analysis

The scanning electron microscopy (SEM) analysis shown in Figure. 6 was carried out by coating the samples with Pt to reduce charging induced distortion. From the SEM images, the diameter of the Fe-BDC-DMF particles can be estimated. The powder, as analyzed by SEM, is mostly distributed as small agglomerated particles from 0.140 to 0.559 μm with an average diameter of 0.213 μm.

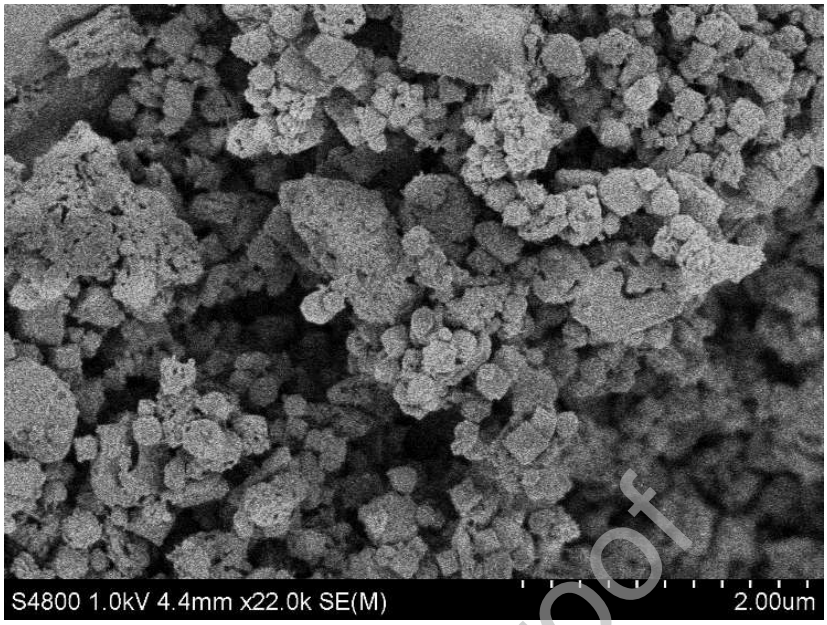

Figure. 6. Scanning electron microscopy (SEM) of the Fe-BDC-DMF powder.

The SEM coupled with energy dispersive spectroscopy (EDS) provides a qualitative elemental and semi quantitative analysis of the Fe-BDC-DMF composition. The EDS spectrum and the elemental composition is presented in Fig. 7.

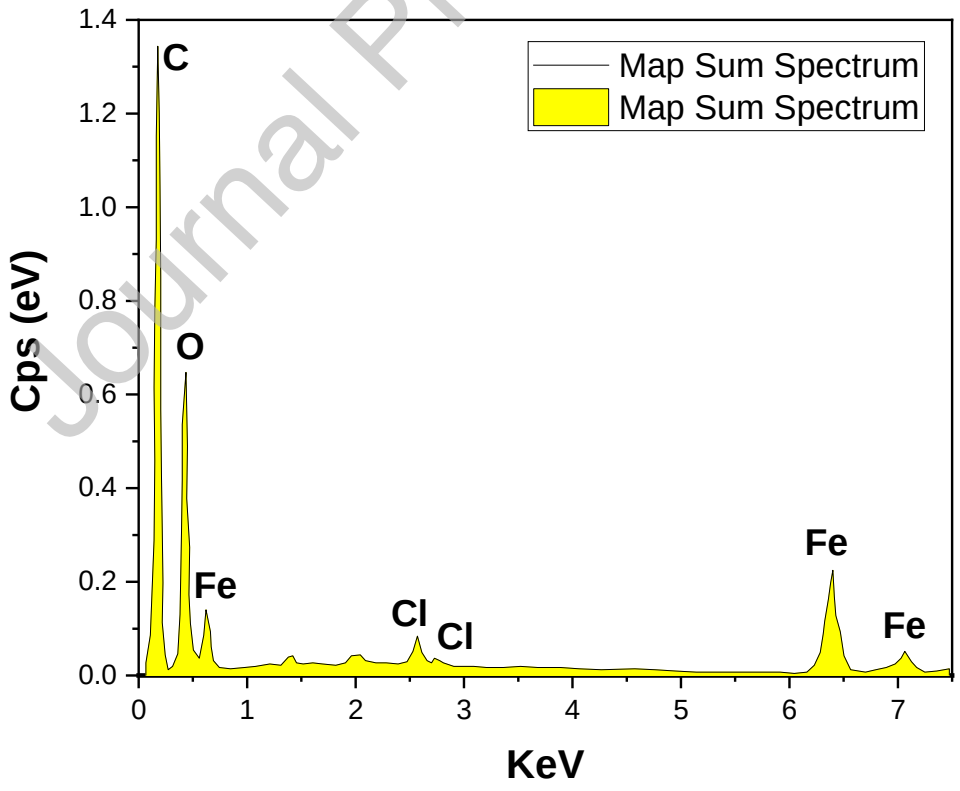

Figure 7. EDS spectrum of the Fe-BDC-DMF powder.

IR Spectroscopy

The FT–IR spectrum of Fe-BDC-DMF in Fig. 8 is consistent with the structural characteristics determined by powder X-ray diffraction shown in Fig. 4. By comparing the IR spectra of terephthalic acid (H_2BDC) and Fe-BDC-DMF, the coordination parts of the ligand bond to the Fe^{3+} ion were explored. In the mixture, the stretching vibrations for the ν(C=O) and ν(C-O) bonds show a significant shift from 1648 to 1633 cm^{-1} and from 1204 to 1167 cm^{-1} for terephthalic acid. The absorptions between 2964 and 2855 cm^{-1} are characteristic of the C-H aromatic and aliphatic stretching vibrations for both structures. The absorptions between 729 and 696 cm^{-1} are characteristic of aromatic ring torsion vibrations for both structures. The range of 579-635 cm^{-1} corresponds to the vibration of the ν(Fe-O) bonds and two bands of ν(Fe-OH) were identified at 1609 and 3369 cm^{-1}, representing the stretching vibration of the hydroxyl groups in the Fe-BDC-DMF [29]. The absorptions between 3500 and 3000 cm^{-1} are characteristic of the O-H hydrogen bond stretching vibrations for the H_2BDC but in the Fe-BDC-DMF its signal disappear due to the formation of the Fe-O bonds.

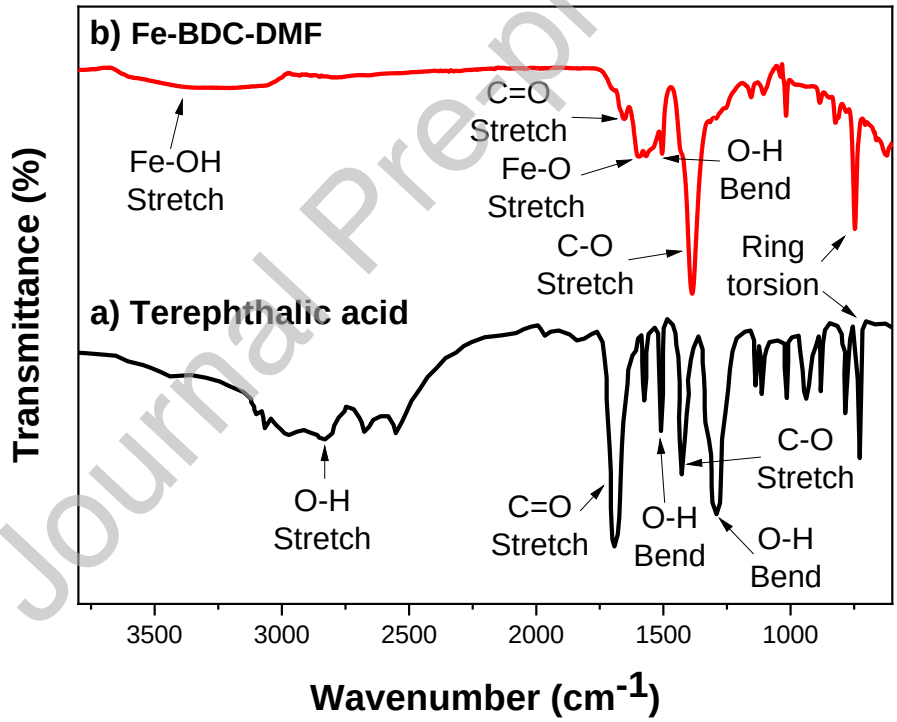

Figure 8. The IR spectra of (a) terephthalic acid (H_2BDC) black line and (b) Fe-BDC-DMF red line.

Electrochemical properties

The electrochemical performance of the synthetized Fe-BDC-DMF mixture versus Li^+/Li^0 was evaluated by cyclic voltammetry (CV) in the potential window 0.5−3.5 V to identify the redox processes by six successive CV scans, as shown in Fig. 9. The experimental data reveal the

intercalation peaks and the formation of a solid electrolyte interphase (SEI). After the first scan, subsequent cycles are stable with only small decay in intensity.

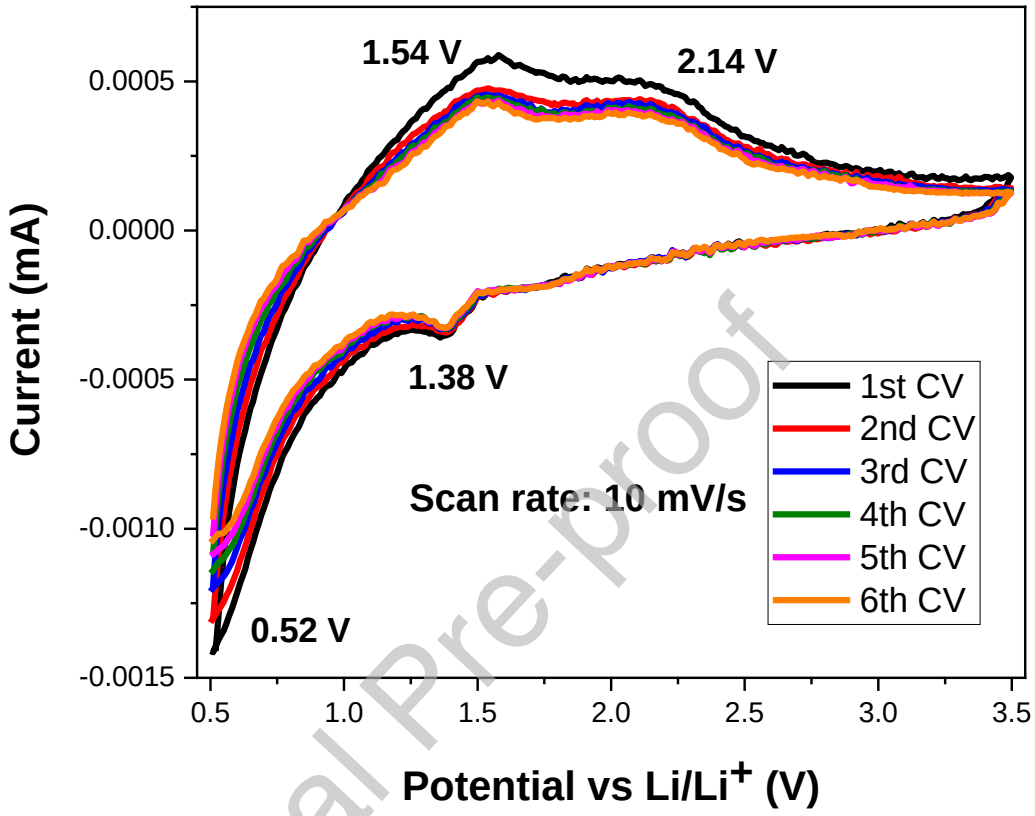

Figure 9. Cyclic voltammograms of Fe-BDC-DMF at potential window of 0.5-3.5 V, T=20 °C, 1M $LiPF_6$ dissolved in EC-DMC (1:1 vol) as electrolyte, Celgard as a separator.

The peaks at 1.38 and 2.14 V are ascribed to the reversible formation of Li-FeO-, Reaction 2, and the Li^+ insertion in the structure during the first discharge.

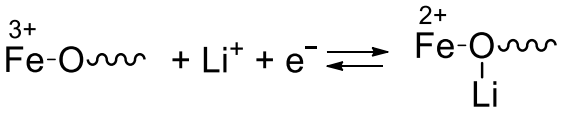

(2)

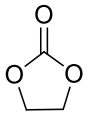

$$+ 2Li^+ + 2e^- \longrightarrow Li_2O + CO_2 + C_2H_4 \quad (3)$$

The peak at 0.52 V correspond also to the formation of amorphous Li_2O according to Reaction 3. and the subsequent formation of the solid-electrolyte interphase (SEI) layer [30]. This reaction decreases the capacity of the material during the first 6 cycles. The peaks at 0.52 V and 1.54 V

correspond to Reaction 4, attributed to the oxidation and reduction of $(C_8H_4O_4)^{2-}$ in the structure being positioned at the expected potentials.

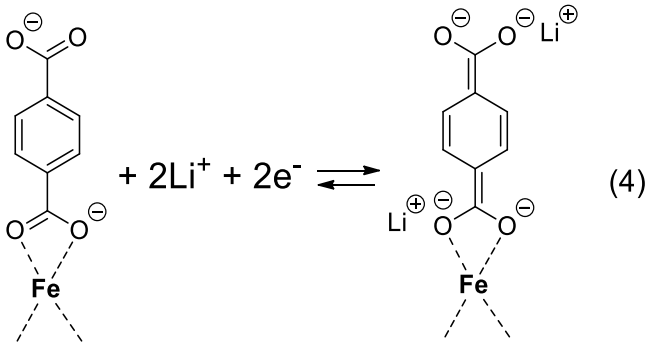

(4)

The conjugated carboxylates containing lithium [30-31] are considered as weakly electron withdrawing ligands. They can act as redox centers for coordination of Li^+ with $-COO^-$. Therefore, it is likely that redox participation of the organic ligand through the COO− groups plays an important role for Li^+ insertion and extraction in the structure.

The channels of the different phases are shown in Fig. 10. They were calculated using Mercury Software [32], using a probe radius of 0.75 Å and a grid spacing of 0.2 Å, and by calculating the voids using the contact surface. The transport of the Li^+ ions in the insertion and deinsertion process are through the empty spaces (voids) in the structure. These pore channels provide a conduction pathway for the Li^+ ions through the structure of the Fe-BDC and leads to a low resistance for ion transfer.

It is possible identify the cavities that provide possible sites for the insertion of Li^+ and the sites for the coordination of Li^+ with the aromatic ring. In order to study the occupation of the Li^+ ions in the structure, the cavities of the different phases were investigated by calculations using CrystalMaker Software [33]. The sites were identified using a "Cavitie search" with 0.75 Å as minimum radius, which correspond to the ionic radius of Li^+ ions. Fig. 9 shows the different sizes of cavities in the structure represented by yellow spheres.

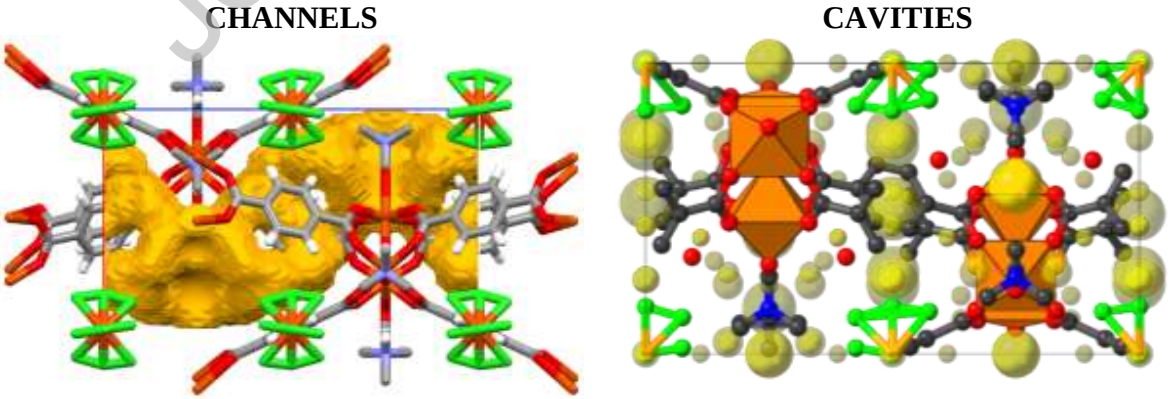

Phase 1 ($[Fe_3O(1,4\text{-}BDC)_3(DMF)_3][FeCl_4]*(DMF)_3$)

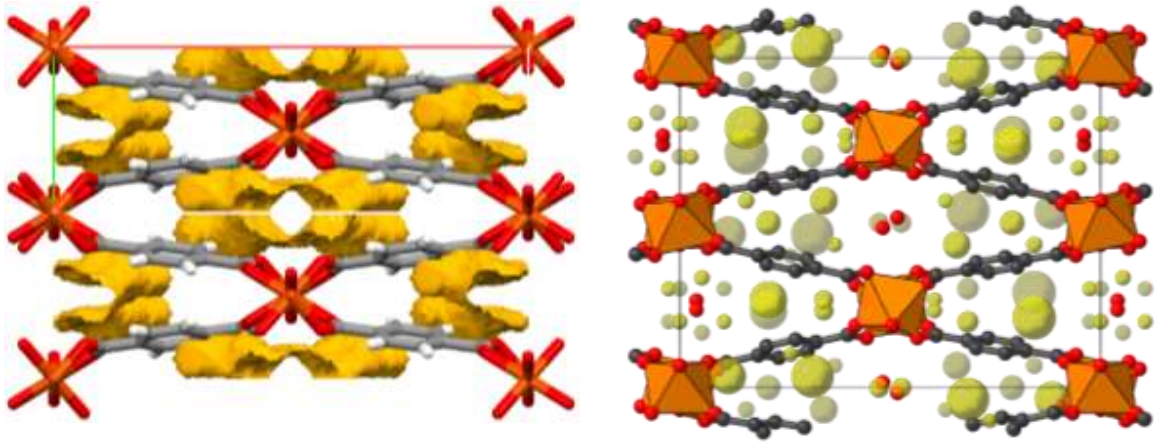

Phase 2 ($Fe^{III}(OH)\{O_2C\text{-}C_6H_4\text{-}CO_2\}$)

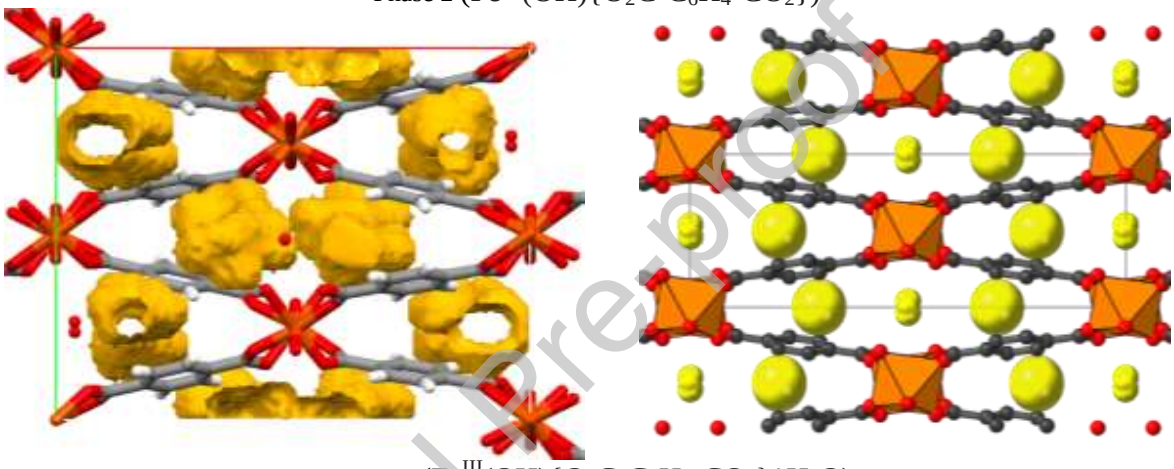

Phase 3 ($Fe^{III}(OH)\{O_2C\text{-}C_6H_4\text{-}CO_2\}*H_2O$).

Figure 10. Illustration of the channels for Li^+ ion diffusion and cavities for Li^+ insertion.

Further work is necessary to understand the exact electrochemical mechanism for Li^+ insertion. According to the calculated structures shown in Fig. 11, there are two possible types of interaction sites for Li^+ insertion in the cavities of Phase 2 and Phase 3. The first interaction is Li^+-O around the oxygen bonded with the Fe^{3+}. The second is Li^+--π interaction. The results for the Phase 2 and Phase 3 can be compared with the results obtained by Combelles et al. [34], who suggested four positions available for Li^+ ions. They used DFT calculations to determine the different sites accessible for Li^+ ions using an algorithm with spherical particles for the solvent to probe the accessible surface area of the porous material and assuming the Li^+ ions had a radius of 1.0 Å. The results of our calculations are similar to those obtained by Combelles et al [34]. The oxygen atom in the carboxylate can attach one Li^+ and each aromatic ring can accommodate one Li^+ ion, which likely is reversibly coordinated with the aromatic ring. This possibly explains the decrease in capacity of the material if the aromatic moieties are collapsing as has been found by Reddy and Sastry [35].

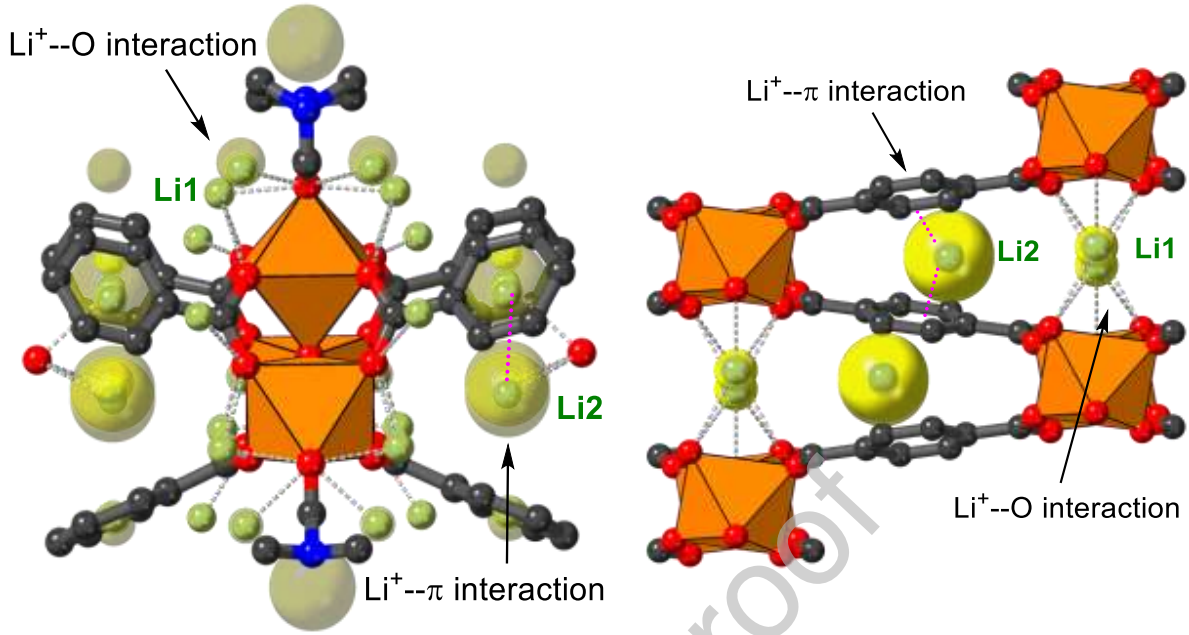

Possible sites for occupation of the Li^+ and its interactions in the structure of 1, 2 and 3

Figure 11. Two crystallographic sites Li1 and Li2 for possible lithium insertion.

The observed irreversible capacity loss can be attributed to increased side reactions with the electrolyte and formation of a thicker SEI layer, and the remaining coordination of Li^+ with the aromatic ring, Fig. 11.

The Nyquist plot in Fig. 12 from impedance spectroscopy measurement shows that the Fe-BDC as assembled has a series resistance of 15.1 Ω and a charge transfer resistance of 275 Ω in the first semicircle and 1.15 kΩ in the second semicircle. After 100 cycles the series resistance has decreased to 6.75 Ω and a single semicircle with a charge transfer resistance of 270 Ω can now be observed. The values are given in Table 2.

Table 2. Data for Impedance Spectra at Different Cycling Stages

State	R1 (Ohm)	R2 (Ohm)	R3 (Ohm)
As assembled (OCP) (Charged)	15.1	275.0	1150
After 100 cycles (Charged)	6.75	270.0	-

The low resistance and charge transfer resistance are an advantage for lithium-ion batteries application as they facilitate easy ion transfer from electrolyte via the surface to the bulk of the active material.

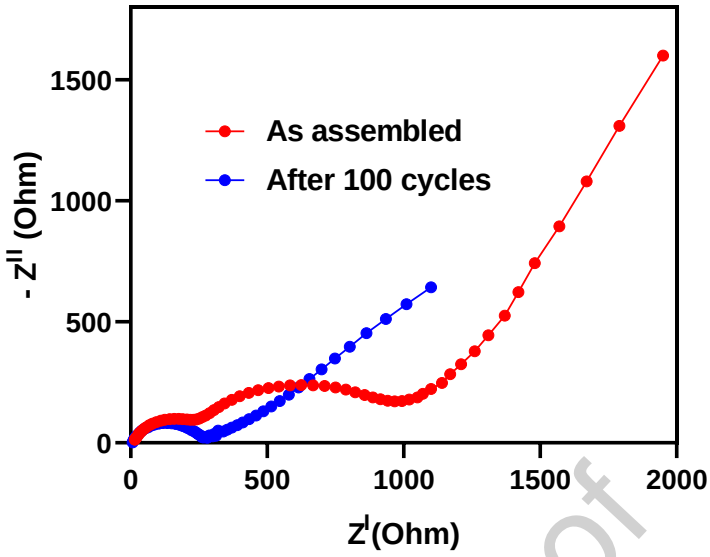

Figure 12. Nyquist plot of the Fe-MOF-DMF half-cell in the frequency range of 300 kHz to 1 mHz with peak to peak amplitude of 10 mV.

The good conductivity of Fe-BDC-DMF can be attributed to pore channels that provide a conduction pathway, and the conducting nature of the Fe-BDC-DMF which leads to a low resistance for ion transfer, Fig. 13. The semicircle at high frequencies in the EIS spectrum can be ascribed to the electrolyte resistance and the surface film impedance and the semicircle at lower frequencies can be ascribed to the lithium-intercalation process. This second semicircle could therefore be described by a reversible charge adsorption [36]. The adsorption and desorption of charge might account for the observed behavior. The charge carriers in the electrolyte arrive at electrode, they can (1) accumulate in the surface of Fe-BDC-DMF or (2) adsorb onto (desorb from) the electrode into the structure of Fe-BDC-DMF.

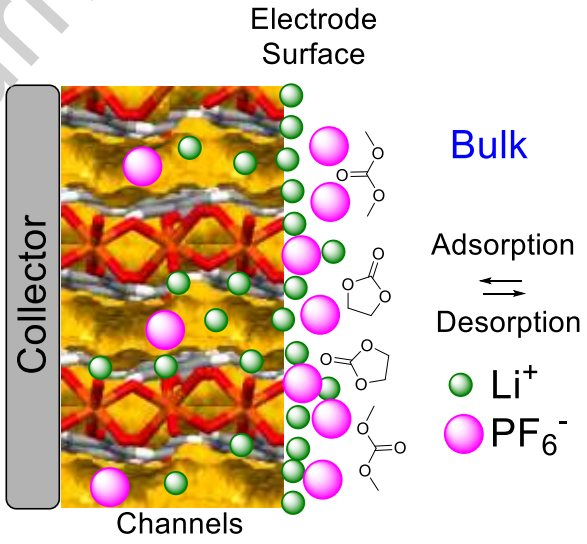

Figure 13. The adsorption and desorption of charge in the Fe-BDC.

The charge−discharge capacity and coulombic efficiency and voltage profiles observed in the potential range of 0.5−3.5 V of the Fe-BDC-DMF electrode are shown in the Figs. 14 and 15. The cycling was performed with a current density of 30 mA/g. The first cycle discharge capacity of the Fe-BDC-DMF electrode is 310 mAh/g, but the discharge capacity of the second cycle has decreased to 275 mAh/g. Thus, a capacity loss of 11% is observed between the first and second cycles. However, after about forty cycles, the Fe-BDC-DMF electrode demonstrates a stable capacity for reversible lithium storage of about 175 mAh/g, indicating good cycling stability of the Fe-BDC-DMF electrode.

Our data are supported by results reported in the literature. The 3D compound $Fe^{III}(OH)_{0.8}F_{0.2}[O_2C–C_6H_4–CO_2]$, [37-38], has a reported capacity of 70 mAh/g. The compound is stable during lithium-ion insertion and extraction and shows a similar structure as of Phase 2 and Phase 3 in our study. The compound $[Fe_3O(BDC)_3(H_2O)_2(NO_3)]_n$ (Fe-MIL-88B), [39-40] with a reported capacity of 144.5 mAh/g, tested at 60 mA/g, shows a similar structure with the trinuclear Fe_3O- cluster in $[Fe_3O(1,4\text{-}BDC)_3(DMF)_3][FeCl_4]*(DMF)_3$.

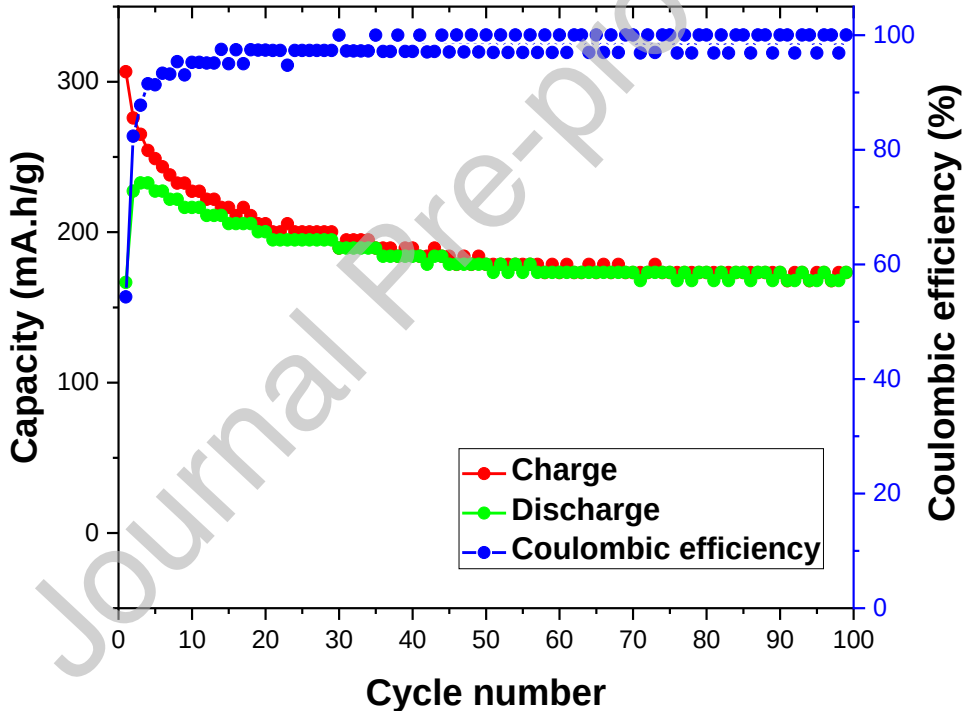

Figure 14. Charge-discharge cycling performances for the Fe-BDC at 30 mA/g.

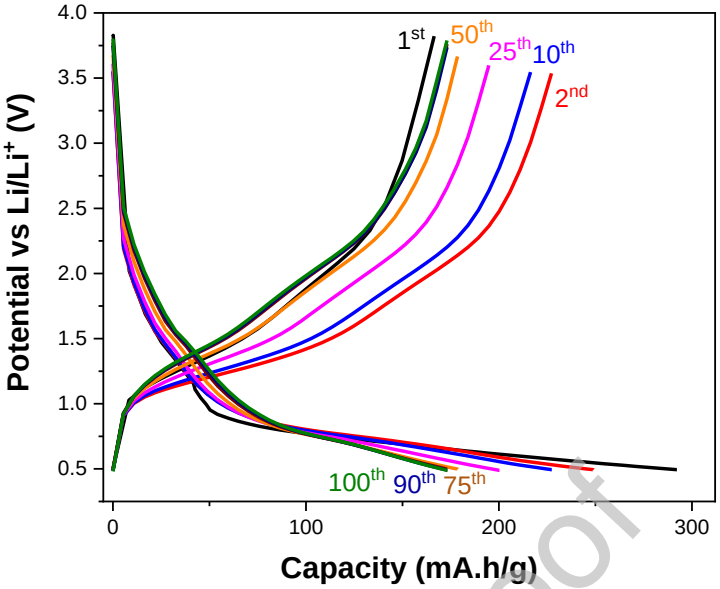

Figure 15. Cell voltage as a function of specific capacity obtained by charging and discharging at 30 mA/g.

5. CONCLUSION

The synthesized MOF, Fe-BDC-DMF, exhibite a good electrochemical behavior when applied as anode material in a lithium-ion battery cell. It shows a high irreversible capacity in the first discharge process and a reversible lithium storage capacity of about of 175 mAh/g at 30 mA/g after forty cycles.

The Fe-BDC-DMF is a mixture of three phases. These phases can be applied as anode material in a lithium-ion battery. The activity of the different active phases has been identified. The Fe-BDC is stable during lithium-ion insertion and extraction. It is possible to obtain one phase by the control of the ratio of the reactants and the conditions of the reaction.

The Fe-BDC-DMF shows a capacity of 350 mAh/g. This is high compared with $Fe^{III}(OH)_{0.8}F_{0.2}[O_2C–C_6H_4–CO_2]$ and we attribute this to the Phase 1 in the Fe-BDC-DMF. The high capacity and good cycling stability confirm the advantages of Fe-MOF-253, Fe-MIL-53 and Fe-MIL–88 B as the electrode materials of a lithium-ion battery. It should be possible to further improve the stability of the material if the amount of Phase 3 formed during synthesis could be minimized, since Phase 1 and Phase 2 do not show any significant changes in the structure in the charge-discharge processes. However, further investigations to study the relation between structure and redox processes are needed to fully characterize this interesting material.

CRediT author statement

Cesario Ajpi: Synthesis, Design, Experimental work, Conceptualization, Methodology, Software, Structure characterization, Electrochemical characterization, Data analysis, Writing-paper. Writing-Original draft preparation,

Validation, Visualization and Investigation. **Naviana Leiva:** synthesis, Electrochemical characterization, design and experimental work. **Anders Lundblad:** Supervision, Validation, Writing-Reviewing and Editing, **Göran Lindbergh:** Supervision, Validation, Writing-Reviewing and Editing, **Saul Cabrera:** Supervision, Validation, Writing-Reviewing and Editing.

Declaration of Interest Statement

We wish to confirm that there are no known conflicts of interest associated with this publication.

Acknowledgements

This work is dedicated to the late Prof. Saul Cabrera. This work was supported by the SIDA (Swedish International Development Agency), KTH Royal Institute of Technology, UMSA (Universidad Mayor de San Andres) in collaboration with IIQ (Chemical Research Institute), Department of Inorganic Chemistry and Materials Science/Advanced Materials. The authors would also like to thank Alexander J. Smith for helping to improve the language of the article.

Funding information

Funding for this research was provided by: SIDA (Swedish International Development Agency); KTH Royal Institute of Technology, Department of Chemical Engineering, Applied Electrochemistry; UMSA Universidad Mayor de San Andres, Department of Inorganic Chemistry and Materials Science/Advanced Materials, IIQ Chemical Research Institute.

REFERENCES

1) Makoto Nanko; Definitions and categories of hybrid materials, Adv.in Tech.of Mat and Mat Proc. J. (2009) (ATM, IS SN 1440-0731), Vol 11 [1] 1−8.
2) H. K. Chae, D. Y. Siberio-Pe´ rez, J. Kim, Y. Go, M. Eddaoudi, A. J. Matzger, M. O'Keeffe and O. M. Yaghi, Nature (2004), 427, 523.
3) G.Ferey, C. Mellot-Draznieks, C. Serre, F. Millange, J. Dutour, S. Surble and I. Margiolaki, Science (2005), 309, 2040.
4) N. L. Rosi, J. Eckert, M. Eddaoudi, D. T. Vodak, J. Kim, M. O'Keeffe and O. M. Yaghi, Science (2003), 300, 1127.
5) X. Lin, J. Jia, P. Hubberstey, M. Schroder and N. R. Champness, CrystEngComm (2007), 9, 438.
6) M. Latroche, S. Surble´ , C. Serre, C. Mellot-Draznieks, P. L. Llewellyn, J.-H. Lee, J.-S. Chang, H. J. Sung and G. Fe´rey, Angew. Chem., Int. Ed. (2006), 45, 8227.
7) A. R. Millward and O. M. Yaghi, J. Am. Chem. Soc. (2005), 127, 17998.

8) S. Bourrelly, P. L. Llewellyn, C. Serre, F. Millange, T. Loiseau and G. Fe´rey, J. Am. Chem. Soc.(2005), 127, 13519.
9) G. Ferey, F. Millange, M. Morcrette, C. Serre, M. L. Doublet, J. M. Grene`che and J. M. Tarascon, Angew. Chem., Int. Ed., (2007), 46, 3259.
10) Kirandeep, Sushila, Aashima Sharma, Subhash Chandra Sahoo, Girijesh Kumar, Surinder Kumar Mehta, Ramesh Kataria, Synthesis and characterization of 1D-Co/Zn MOFs having potential for efficient dye adsorption from wastewater, Journal of Molecular Structure, Volume 1226, Part A, 2021, 129327, ISSN 0022-2860
11) Kirandeep, Ajay Kumar, Aashima Sharma, Subash Chandra Sahoo, Ennio Zangrando, Vikram Saini, Ramesh Kataria, Surinder Kumar Mehta, Metal organic framework as "turn-on" fluorescent sensor for Zr(IV) ions and selective adsorbent for organic dyes, Microchemical Journal, Volume 171, 2021, 106824, ISSN 0026-265X,
12) Kirandeep, Ahmad Husain, Ajit Kumar Kharwar, Ramesh Kataria, and Girijesh Kumar, Co(II)-based Metal–Organic Frameworks and Their Application in Gas Sorption and Solvatochromism, Cryst. Growth Des. 2019, 19, 3, 1640–1648.
13) C. Serre, F. Millange, C. Thouvenot, M. Nogues, G. Marsolier, D. Louer and G. Fe´rey, J. Am. Chem. Soc., (2002), 124, 13519.
14) Sun, Z., Yang, M., Ma, Y. & Li, L. C. Cryst. Growth Des. (2017). 17, 4326–4335.
15) Zhang, L. Y., Lu, L. P., Zhu, M. L. & Feng, S. S.. CrystEngComm, (2017), 19, 1953–1964.
16) Zhou, T., Zhou, R.-J. & An, Z. (2009). Acta Cryst. E65, m779.
17) Bendjellal, N., Trifa, C., Bouacida, S., Boudaren, C., Boudraa, M. & Merazig, H. (2018). Acta Cryst. C74, 240-247.
18) Huang, W., Zhang, J., Li, J. & Zhang, C. Acta Cryst. (2013). C69, 123–126.
19) Tao, C. L., Chen, B. C., Liu, X. G., Zhou, L. J., Zhu, X. L., Cao, J., Gu, Z. G., Zhao, Z. J., Shen, L. & Tang, B. Z.. Chem. Commun. (2017) 53, 9975–9978.
20) Camilla Scherb, Alexander Schödel, Thomas Bein, Directing the Structure of Metal–Organic Frameworks by Oriented Surface Growth on an Organic Monolayer, J. German chemical society, (2008), Volume47, Issue31, July 21, 5777-5779.
21) Le, T.X.H.; Cowan, M.G.; Drobek, M.; Bechelany, M.; Julbe, A.; Cretin, M. Fe-Nanoporous Carbon Derived from MIL-53(Fe): A Heterogeneous Catalyst for Mineralization of Organic Pollutants. Nanomaterials 2019, 9, 641.
22) Navarathna, C.M., Dewage, N.B., Karunanayake, A.G. et al. Rhodamine B Adsorptive Removal and Photocatalytic Degradation on MIL-53-Fe MOF/Magnetic Magnetite/Biochar Composites. J Inorg Organomet Polym 30, 214–229 (2020).
23) Chen, Dezhi and Chen, Shasha and Jiang, Yijie and Xie, Shasha and Quan, Hongying and Hua, Li and Luo, Xubiao and Guo, Lin, Heterogeneous Fenton-like catalysis of Fe-MOF derived magnetic carbon nanocomposites for degradation of 4-nitrophenol, ***RSC Adv.***, 2017,**7**, 49024-49030
24) Xuan Qiu, Xi Wang and Yingwei Li, Controlled growth of dense and ordered metal–organic framework nanoparticles on graphene oxide, Chem. Commun., 2015, 51, 3874.
25) Yongchao Jiang, Haitao Zhao, Luchao Yue, Jie Liang, Tingshuai Li, Qian Liu, Yonglan Luo, Xiangzhe Kong, Siyu Lu, Xifeng Shi, Kun Zhou, Xuping Sun, Recent advances in

lithium-based batteries using metal organic frameworks as electrode materials, Electrochemistry Communications, Volume 122, 2021, 106881, ISSN 1388-2481.

26) Yang, Qingyun and Liu, Yanjin and Ou, Hong and Li, Xueyi and Lin, Xiaoming and Zeb, Akif and Hu, Lei,"Fe-Based metal–organic frameworks as functional materials for battery applications", Inorg. Chem. Front. 2022, 9, 5, 827-844.
27) Andrea C. Sudik, Adrien P. Cote, and Omar M. Yaghi, Metal-Organic Frameworks Based on Trigonal Prismatic Building Blocks and the New “acs” Topology, Inorg. Chem. (2005), 44, 9, 2998-3000.
28) Franck Millange, Nathalie Guillou, Richard I. Walton, Jean-Marc Greneche, Irene Margiolakidand Gerard Ferey, Effect of the nature of the metal on the breathing steps in MOFs with dynamic frameworks, Chem. Commun., (2008), 4732-4734.
29) A. A. Javidparvar; B. Ramezanzadeh; E. Ghasemi, The effect of surface morphology and treatment of Fe3O4 nanoparticles on the corrosion resistance of epoxy coating, Journal of the Taiwan Institute of Chemical Engineers, ISSN: 1876-1070, Vol: 61,356-366.
30) Armand M, Grugeon S, Vezin H, Laruelle S, Ribière P, Poizot P, Tarascon JM., Nat Mater. (2009), Feb; 8(2):120-5.
31) Sandipan Maiti, Atin Pramanik, Unnikrishnan Manju and Sourindra Mahanty (2015). ACS Appl. Mater. Interfaces, 7, 16357−16363.
32) Macrae, C. F., Edgington, P. R., McCabe, P., Pidcock, E., Shields, G. P., Taylor, R., Towler, M. & van de Streek, J. J. Appl. Cryst. (2006). 39, 453-457.
33) Palmer, D. C. (2014). CrystalMaker. CrystalMaker Software Ltd, Begbroke, Oxfordshire, England.
34) C. Combelles, M. Ben Yahia, L. Pedesseau, M.-L. Doublet, FeII/FeIII mixed-valence state induced by Li-insertion into the metal-organic-framework MIL-53(Fe): A DFT+U study, Journal of Power Sources 196 (2011) 3426–3432.
35) A. Srinivas Reddy and G. Narahari Sastry, Cation [M = H+, Li+, Na+, K+, Ca2+, Mg2+, NH4+, and NMe4+] Interactions with the Aromatic Motifs of Naturally Occurring Amino Acids: A Theoretical Study, The Journal of Physical Chemistry A (2005) 109 (39), 8893-8903.
36) Benjamin A. Yezer, Aditya S. Khair, Paul J. Sides, Dennis C. Prieve, Determination of charge carrier concentration in doped nonpolar liquids by impedance spectroscopy in the presence of charge adsorption, Journal of Colloid and Interface Science 469 (2016) 325–337.
37) Gérard Férey, Franck Millange, Mathieu Morcrette, Christian Serre, Marie-Liesse Doublet, Jean-Marc Grenèche, Jean-Marie Tarascon, Mixed-Valence Li/Fe-Based Metal–Organic Frameworks with Both Reversible Redox and Sorption Properties,46,18, (2007), Pages 3259-3263.
38) F.Millange, G.Férey, M. Morcrette, C. Serrea, M-L.Doublet, J-M.Grenèche, J-M.Tarascon, Towards the reactivity of MIL-53 or FeIII(OH)0.8F0.2[O2C-C6H4-CO2] versus lithium, Studies in Surface Science and Catalysis, 170, (2007),2037-2041.
39) Lisha Shen, Huawei Songa, Chengxin Wang, Metal-Organic Frameworks Triggered High-Efficiency Li storage in Fe-Based Polyhedral Nanorods for Lithium-ion Batteries, Electrochimica Acta, 235, (2017),595-603.

40) Xuechao Cai, Jun Lin, and Maolin Pang, Facile Synthesis of Highly Uniform Fe-MIL-88B Particles, Cryst. Growth Des. 2016, 16, 7, 3565–3568.